Author/s:
Syeda, W;Blunck, Y;Kolbe, S;Cleary, JO;Johnston, LA

Title:
A continuum of T2* components: Flexible fast fraction mapping in sodium MRI

Date:
2019-06-01

Citation:
Syeda, W., Blunck, Y., Kolbe, S., Cleary, J. O. & Johnston, L. A. (2019). A continuum of T2* components: Flexible fast fraction mapping in sodium MRI. Magnetic Resonance in Medicine, 81 (6), pp.3854-3864. https://doi.org/10.1002/mrm.27659.

A Continuum of T_2^* Components: Flexible Fast Fraction Mapping in Sodium MRI

Running title:

Flexible Fast Fraction Mapping in Sodium MRI

Warda Syeda[1*], Yasmin Blunck[1,2], Scott Kolbe[1], Jon O. Cleary[1], Leigh A. Johnston[1,2]

[1]Melbourne Brain Centre Imaging Unit, The University of Melbourne, Australia

[2]Department of Biomedical Engineering, The University of Melbourne, Australia

December 22, 2018

*Correspondence: Melbourne Brain Centre Imaging Unit, Kenneth Myer Building, University of Melbourne, 30 Royal Parade, Parkville VIC 3052, Australia

email: wtsyeda@gmail.com

Keywords: Sodium MRI, gamma distribution, statistical modelling, continuum model, transverse relaxation decay

Word count: 4000 (approx)

Abstract

Purpose: Parameter mapping in sodium MRI data is challenging due to inherently low SNR and spatial resolution, prompting the need to employ robust models and estimation techniques. This work aims to develop a continuum model of sodium T_2^*- decay to overcome the limitations of the commonly employed bi-exponential models. Estimates of mean T_2^*- decay and fast component fraction in tissue are emergent from the inferred continuum model.

Methods: A closed-form continuum model was derived assuming a gamma distribution of T_2^* components. Sodium MRI was performed on four healthy human subjects and a phantom consisting of closely packed vials filled with an aqueous solution of varying sodium and agarose concentrations. The continuum model was applied to the phantom and in vivo human multi-echo 7T data. Parameter maps by voxelwise model-fitting were obtained.

Results: The continuum model demonstrated comparable estimation performance to the bi-exponential model. The parameter maps provided improved contrast between tissue structures. The fast component fraction, an indicator of the heterogeneity of localised sodium motion regimes in tissue, was zero in CSF and high in WM structures.

Conclusion: The continuum distribution model provides high quality, high contrast parameter maps, and informative voxelwise estimates of the relative weighting between fast and slow decay components.

1 Introduction

Sodium (^{23}Na) is an important electrolyte present in living organisms, vital for cell integrity, cohesion and function (1, 2). It plays a crucial role in the nervous system, neuronal transmission via action potentials is carried out through opening and closing of ^{23}Na gated ion channels and resting membrane potential is restored through active transport of sodium out of the cell through the sodium-potassium pump (3). Pathological conditions such as cardiovascular disease (4, 5), impaired renal function (6), neurological disorders (7, 8), diabetes and other metabolic disorders (9, 10) have been associated with alterations in local sodium concentration.

With a nuclear moment of 3/2, ^{23}Na is NMR observable and gives rise to the second strongest NMR signal in the human body. The MR signal in biological tissue from ^{23}Na nuclei is roughly four orders of magnitude weaker than that of the ^{1}H MR signal (11), making it challenging to obtain a viable ^{23}Na MR signal at low field strengths. Recent advances in high field MR imaging and hardware design have led to acquisition protocols and analysis techniques tailored for imaging ^{23}Na. Thus to date there have been a wide variety of sodium MRI studies assessing developmental and pathophysiological processes including, but not limited to, neurogenerative diseases (12, 13, 14, 15), tumours (16, 17, 18, 19), stroke (20), multiple sclerosis

(21, 22), Alzheimer's disease (23), Huntington's disease (24), breast cancer (25), acute myocardial infraction (26, 27, 28, 29), diabetes (30), osteoarthritis (31), and nephropathy (32).

Given the objective for sodium MRI to produce robust biomarkers of disease and disorder, accurate quantification of ^{23}Na concentration and relaxation properties is essential. The estimation of the transverse relaxation rate from multi-echo sodium MRI data is challenging, both due to the low SNR of sodium images, and the complex magnetic dipole and electric quadrupole coupling in tissue micro-environments. In fast motion regimes, such as liquids, the electric field gradients at sodium nuclei motionally average out, giving rise to mono-exponential transverse relaxation decay (33). Presence of local macromolecular charges in more heterogeneous slow motion environments, such as tissue, causes non-vanishing electric field gradients at sodium nuclei, resulting in bi-exponential transverse relaxation (33). In biological structures, ^{23}Na exists in various compartmentalized heterogeneous states such as ^{23}Na ions in fast motion regimes, ^{23}Na under varying degree of influence from macromolecules, and diffusing and exchanging ^{23}Na ions in restricted anisotropic motion regimes (34, 35, 36).

Typically, a bi-exponential model (BE) is fit to the signal under the assumption of a single sodium compartment, with the fast and slow signal fractions corresponding to satellite and central spin transitions. The signal fractions are either kept variable (37) or constrained to a 60/40 ratio based on ^{23}Na spin dynamics (38, 39, 40). In the recent 3D-MERINA sequence for efficient multi-echo sodium MRI acquisition, a bi-exponential mixture (BEM) approach to fitting the decay model was proposed (39). The BEM approach is a two-step procedure, firstly fitting a BE model, again constrained to the 60/40 ratio in brain tissue, and secondly replacing the BE with a mono-exponential (ME) fit in regions found to be implausible for a two-component BE fit, namely CSF. Both the BE and BEM approaches result in parameter maps that fail to clearly differentiate between white matter (WM) and gray matter (GM), and suffer from a low contrast and signal to noise ratios. Further, the T_2^* estimates of BEM model intrinsically depend on the chosen plausibility threshold, which may vary across acquisition setups and fitting routines.

In reality multiple sodium compartments with varying motion regimes exist in tissue, with each compartment described by two-component transverse relaxation contributing to the observed signal (34). Berendsen et al. observed a strong influence of molecular order present in the tissue sample and the diffusion of sodium ions between different compartments on the averaged quadrupolar interactions, and cautioned against incorrectly attributing two components obtained from bi-exponentially relaxing spins in a single ^{23}Na compartment to 'free' and 'bound' components of ^{23}Na ions (34). Therefore fixing the component fractions removes the flexibility to model relative contributions of the compartmentalized local motion regimes in the ^{23}Na MR signal, and might lead to possible misinterpretation of the underlying biophysical processes that give rise to the sodium transverse relaxation decay.

Rather than constraining the signal model to maintain the 60/40 ratio between fast and slow decay components, we consider a continuum of T_2^* components, based on the premise that sodium exists in the brain in heterogeneous states within localised environments. The idea of a continuum of T_2^* components has recently been explored in a non-parametric approach, where a multimodal continuous distribution of T_2^* is estimated through a regularized inverse Laplace transform (40). In contrast, we employ a parametrised continuum model of T_2^* decay. Our approach makes three key contributions to ^{23}Na-MRI parameter mapping: 1) The continuum model produces T_2^* maps with vastly superior tissue contrast; 2) Parameter estimation is a robust one-step procedure that obviates the use of mixture models; 3) Estimates of fast and slow component fractions are emergent from the inferred continuum model. Indeed, our in vivo human experimental results support the 60/40 split on average in brain tissue, while permitting localised variation that offers a richer source of information than the constrained alternative.

2 Theory

2.1 Models for Transverse ^{23}Na Decay Signal

Bi-exponential Mixture Model

The BEM model employed in (39) to obtain two-compartment parameter mapping from multi-echo ^{23}Na decay signal is presented here for the sake of comparison and reference. The BEM model assumes a two-component exponential decay signal, attributed to satellite and central transitions caused by complex quadrupolar and dipole interactions of sodium spin systems in slow motions regimes (41),

$$M^{BE}(t; M_0,\ T^*_{2_{\text{short}}},\ T^*_{2_{\text{long}}}) = M_0 \left[0.6 \exp\left(-\frac{t}{T^*_{2_{\text{short}}}}\right) + 0.4 \exp\left(-\frac{t}{T^*_{2_{\text{long}}}}\right)\right], \quad [1]$$

where t is the echo time, $T^*_{2_{\text{short}}}$, $T^*_{2_{\text{long}}}$ are the short and long T_2^* decay parameters and M_0 is the signal at the first echo, t_0.

In liquid media, short correlation time compared to the Larmor period result in mono-exponential transverse decay, with signal contributions dominated by the central dipole interactions (41):

$$M^{ME}(t; M_0,\ T^*_{2_{\text{long}}}) = M_0 \exp\left(-\frac{t}{T^*_{2_{\text{long}}}}\right), \quad [2]$$

The procedure employed in (39) to apply the BEM model is to first fit a voxelwise BE model, followed by a plausibility check to ensure that both $T^*_{2_{\text{short}}}$ and $T^*_{2_{\text{long}}}$ lie in acceptable ranges, as determined by previously

reported values in literature (11). Voxels that fail the plausibility check are classified as CSF and a ME model is fit in order to estimate $T_{2_{\text{long}}}^*$.

Proposed Continuum Model

We posit that the voxelwise observation of the T_2^*-weighted sodium signal decay can be well described by a weighted continuum of components, modelling inhomogeneity in the molecular environment. The measured signal at the echo time, t, is given by the integration of the signal components,

$$M^{GA}(t, R_2^*) = M_0 \int_0^\infty e^{-t/R_2^*}\, p(R_2^*)\, dR_2^*, \qquad [3]$$

where $p(R_2^*)$ is the distribution of the relaxation rates. Our continuous distribution model assumes that the random variable, R_2^*, admits a gamma distribution with shape parameter, k, and scale parameter, ζ:

$$p(R_2^*, k, \zeta) = \frac{1}{\zeta^k \Gamma(k)} R_2^{*k-1} e^{-R_2^*/\zeta}, \qquad [4]$$

where $p(R_2^*, k, \zeta)$ is a valid pdf, that integrates to unity. Conveniently, T_2^* is characterized by an equivalent inverse gamma distribution, $T_2^* \sim \text{Inv-Gamma}(k, \zeta)$. The gamma distribution is selected for its ability to describe a wide range of relaxation rate profiles, positive support (defined only for $R_2^* > 0$), a simple analytic expression for the mean value, and the important fact that it makes the integration in (3) tractable, leading to a closed-form expression for the R_2^* distribution model:

$$M^{GA}(t; M_0,\ \zeta,\ k) = M_0(1 + \zeta\, t)^{-k}, \qquad [5]$$

The mean, $R_{2_{GA}}^* = k\zeta$ and variance, $\nu = k\zeta^2$, of the gamma distribution provide estimates of the location and spread of the relaxation rates. The parameter, $T_{2_{GA}}^*$, defined as the reciprocal of the mean rate, $R_{2_{GA}}^*$, is indicative of the mean T_2^* value in each voxel.

Fast Fraction: We define the fast component fraction, f_{fast}, to be the area under the T_2^* pdf up to a threshold value, $T_{2_{\text{th}}}^*$:

$$f_{\text{fast}} = \int_0^{T_{2_{\text{th}}}^*} p(T_2^*)\, dT_2^*. \qquad [6]$$

Here, we select $T_{2_{\text{th}}}^* = 15$ ms based on the range of fast T_2^* component values in tissue previously reported in the literature (33). In contrast to fixed 60/40 split of T_2^* fast and slow components in the BEM model, the parameter, f_{fast} varies in the range (0-1), conflating the relative contribution of the continuum of fast components below 15ms.

3 Methods

An overview of the image acquisition, post-processing and model-fitting routine is presented in Figure 1. In the following sections we describe each step in the processing routine.

3.1 MRI Experiments

Imaging was performed on a research 7T MRI (Siemens Healthineers, Erlangen, Germany) with a transmit-receive dual-tuned 1H-23Na head coil (QED, Mayfield Village, Ohio, USA). Sodium images were acquired with a radial multi-echo 3D-MERINA acquisition protocol (39) with parameters: TR=160 ms, FA=90°, TRO=2 ms. A total of 38 echoes were acquired with the initial TE=0.4 ms defined as the time interval between the centre of the pulse to ADC onset. Images were acquired over an isotropic field of view of 20 cm and regridded offline in MATLAB onto an isotropic grid with a nominal resolution of 3.1 mm, Prior to acquisition, shimming was performed on the ^{1}H-channel using 10 iterations of an inbuilt shimming procedure. Images were acquired on a phantom with varying concentrations of NaCl and agar, as described in (39), and on four healthy human subjects. All human imaging was conducted with the approval of the University of Melbourne Human Research Ethics Committee, and volunteers gave an informed consent.

Additional proton MRI images were acquired for each human subject. A ^{1}H-FLASH image was obtained with TE=3.06 ms, TR=11 ms, 14° flip angle and 1mm isotropic resolution. Brain tissue segmentation was performed on a 1H-MP2RAGE image acquired at inversion times 700 and 2700 ms, with 5° and 6° flip angles, TE=2.94 ms, TR=4900 ms, GRAPPA factor 4, and isotropic resolution of 0.9 mm. ^{1}H-MP2RAGE were imaged using a 32- channel head coil (Nova Medical Inc., Wilmington MA, USA) in a separate imaging session. Tissue segmentation was performed in FMRIB Software Library v.5.09 (Oxford, U.K.) (42) and involved three main steps: Brain extraction from the FLASH image, registration of brain mask onto MP2RAGE image and tissue segmentation (CSF, GM, WM) of masked MP2RAGE, and the registration of segmented brain regions from the FLASH image onto the ^{23}Na image.

3.2 Parameter Estimation

The estimation of gamma distribution parameters was performed on magnitude images. It is well known that noise is Rician distributed in the foreground (signal) region and Rayleigh distributed in the background (no signal) region (43).

The Rician probability distribution is defined as

$$p_{Rice}(x; M^i, \sigma) = \frac{x}{\sigma^2} e^{-(x^2 + M^{i\,2})/2\sigma^2} I_0\left(\frac{xM^i}{\sigma^2}\right), \quad [7]$$

where I_0 is the modified Bessel function of the first kind, M^i is the signal model, $i \in \{\text{ME, BE, GA}\}$ and σ^2 is the variance of the Gaussian noise in the complex data. In the absence of signal, $M^i = 0$, resulting in the Rayleigh noise distribution,

$$p_{Rayleigh}(x; \sigma) = \frac{x}{\sigma^2} e^{-x^2/2\sigma^2}, \quad [8]$$

with mean, $\mu = \sigma\sqrt{\pi/2}$. The mean of the Rayleigh noise in the background was used to estimate the noise variance, σ^2.

In order to perform parameter estimation, a Rician-distributed log-likelihood function was constructed for Maximum Likelihood (ML) estimation. The ML parameter estimation is a non-linear optimization problem, which was implemented in MATLAB and a constrained nonlinear multivariate solver was used to carry out the optimization. The solver was initialized with fixed $R^*_{2_{GA}} = 150$ ms^{-1}. A high initial value of $R^*_{2_{GA}}$ was found to ensure the nonlinear solver converged to biophysically plausible T_2^* values.

The value of the log-likelihood function at the ML estimate was used as a measure of model-fit quality, as it quantifies the most likely parameter estimates, given the observed data. Voxelwise maps of model likelihood were calculated for both BE and GA models and a paired t-test was performed to compare estimation performance of the models.

4 Results

Phantom Data

The ability of the GA model to discriminate between varying sodium concentrations and viscosities was investigated by the results of mean T_2^* estimation in the phantom data (Figure 2). The parameter maps obtained through voxel-wise fitting are displayed in Figure 2a. The $T^*_{2_{\text{GA}}}$ map shows clear contrast across vials with varying agarose concentration whilst maintaining constancy along sodium concentration, except at the low concentration of 30mM where the map is more speckled. The noisy estimates at low sodium concentration indicate the detrimental effects of low SNR on MLE estimation. In comparison, the $T^*_{2_{\text{short}}}$ and $T^*_{2_{\text{long}}}$ maps from the BEM model are more noisy with limited contrast across vials.

For each phantom vial, the mean estimated $T^*_{2_{\text{GA}}}$ along with the standard deviation showed a clear decreasing trend with increasing agarose concentration (Figure 2b). At low sodium concentration of 30mM/I, the

$T^*_{2_{\mathrm{GA}}}$ estimates were consistently lower whilst maintaining the decreasing trend observed at higher sodium concentrations. Similarly, the fast fraction was zero in liquid and increased with increasing agarose content, as expected. On the contrary, $T^*_{2_{\mathrm{short}}}$ from BEM failed to produce a clear trend across agarose concentration, showing the difficulty of the biexponential models to correctly discern the subtle variations in physical and chemical composition of vial samples.

In liquid vials, the mean $T^*_{2_{\mathrm{GA}}}$ ranged between $36-42$ ms across sodium concentration with zero fast fraction, indicating the absence of short T_2^* components in fluid environments (Figure 2b). The decrease in mean $T^*_{2_{\mathrm{GA}}}$ with emerging fast fraction in more solid environments (3-6% agarose) showed a predominantly short T_2^* component population. Instead of fixed 60/40 split employed in the BEM model, the GA model allowed the fast fraction to vary, thus capturing the effects of localised heterogeneous micro-environments on the sodium decay signal. At 3% agar, the mean f_{fast} at higher sodium concentrations was $\sim$40%, which increased to $\sim$60% in the 6% agar samples.

In vivo Data

For each subject, voxel-wise data from each slice was well fit by the GA model, with distinct R_2^* gamma pdfs obtained in WM, GM and CSF regions of the brain (see Figure 3a-b for an example of single voxel fits in axial slice 36 of subject 1). For these voxels, the mean T_2^* values estimated in predominantly WM and GM voxels were 1ms and 8.5ms, respectively. However, a higher mean T_2^* value of 27ms was estimated in the CSF voxel. Similarly, f_{fast} in these voxels was estimated at 0.83, 0.61 and 0 in WM, GM and CSF, respectively, indicating the different structural compositions of tissue types. The histogram of the voxels from the difference map ML_{GA}-ML_{BE} is centred at zero with a narrow spread, demonstrating comparable estimation performance of both models (Figure 3c). The paired t-test accepted the null hypothesis that the difference, ML_{GA}-ML_{BE}, is a zero-mean Gaussian with $p = 1$.

For all four subjects, the parameter maps generated from the application of BEM and GA models to the experimental sodium MRI data demonstrated the ability of the GA model to provide better contrast in brain tissue regions. Along with distinguishing CSF regions from soft tissue, the $T^*_{2_{\mathrm{GA}}}$ map discerns WM from GM structures, leading to superior contrast with enhanced SNR (Figure 4). Generally, the WM appears darker than the GM, with slightly lower $T^*_{2_{\mathrm{GA}}}$ values. The fast fraction maps provide contrast with enhanced boundaries between different tissue types. In WM regions, f_{fast} was higher than GM regions, while it was zero in CSF region, as expected. In comparison, $T^*_{2_{\mathrm{short}}}$ and $T^*_{2_{\mathrm{long}}}$ maps (Figure 4) show clear boundaries between CSF and tissue, but fail to provide meaningful inter-tissue contrast. Specifically, the $T^*_{2_{\mathrm{short}}}$ map is extremely noisy in tissue with $T^*_{2_{\mathrm{long}}}$ varying randomly from voxel to voxel.

Information in continuum model parameters

ML estimation results were used to empirically obtain the probability distributions of $T^*_{2\,\mathrm{GA}}$ in WM, GM and CSF through histogram normalization. Figure 5a displays the resulting $T^*_{2\,\mathrm{GA}}$ distributions for subject 1. $T^*_{2\,\mathrm{GA}}$ in CSF showed a flat distribution ranging between 20-60 ms, with a few voxels below 20 ms due to partial volume effects in low resolution sodium MRI data. In comparison, $T^*_{2\,\mathrm{GA}}$ in WM and GM regions demonstrated peaked distributions with WM having a lower peak (5ms) than GM (7ms), indicating the efficacy of the GA model in discerning subtle T^*_2 variations across different tissue types.

The empirical probability distributions of fast fraction, f_{fast}, estimated from the GA model estimates provide evidence of the ability of the GA model to capture variations in the volume fractions of short and long T^*_2 components in tissue micro-environments (Figure 5b). The absence of $T^*_{2\,\mathrm{short}}$ component in CSF was revealed by zero f_{fast}, except in voxels with partial volume effects. The mean value of f_{fast} was 0.02 ± 0.07 in CSF, 0.41 ± 0.22 in GM and 0.53 ± 0.21 in WM. Even though the empirical pdfs in WM and GM overlapped, the utility of f_{fast} in discriminating WM and GM regions was demonstrated by separated peaks (0.68 in GM and 0.73 in WM).

Influence of $T^*_{2_{th}}$ on f_{fast} estimates

The choice of $T^*_{2_{\mathrm{th}}}$ directly impacts the resultant f_{fast} estimates (Figure 6). Although the contrast between tissue and CSF is retained at all threshold values, maximal inter-tissue contrast is observed at $T^*_{2_{\mathrm{th}}} = 15$ ms. At a low $T^*_{2_{\mathrm{th}}}$ of 10 ms, f_{fast} in WM is under-estimated, whereas at a high threshold value of 20 ms f_{fast} is over-estimated in GM, resulting in diminished inter-tissue contrast.

5 Discussion

The continuum distribution approach to modelling the sodium signal, based on the gamma distribution, has been shown to be flexible and biophysically plausible, in application to phantom and in vivo human 7T data. The gamma model provides parameter maps with superior contrast than the commonly employed bi-exponential model. Further, the fast T^*_2 fraction provides additional insight into the underlying tissue environment.

Parameter estimation from bi-exponential models is well-known to be difficult (44), and when coupled with the low SNR and poor spatial resolution of sodium MRI data, the application of bi-exponential models become problematic, producing noisier and less informative parameter maps in tissue regions. Assuming a

gamma distribution of T_2^* components, we have derived a closed-form continuous distribution model that gives rise to intuitively meaningful and high quality parameter maps. In liquid media, such as CSF, the ^{23}Na signal is known to comprise of only a long T_2^* component, giving rise to mono-exponential transverse relaxation decay. Bi-exponential models, with their assumption of two distinct T_2^* components, can struggle to fit CSF data, which prompted the two-step estimation technique in (39). The continuum distribution model overcomes this drawback by replacing the rigid two-component assumption with the presence of a continuum of components described by a probability distribution. The additional flexibility offered by the gamma distribution in characterising a wide range of T_2^* distributions allows for straightforward one-step estimation of the gamma model parameters both in CSF and tissue, alleviating the need to apply any plausibility check, and resulting in quantitative parameter maps with enhanced contrast.

The distribution of mean transverse relaxation in Figure 5 has been estimated assuming multi-compartment sodium spin systems, in contrast to previously reported single compartment two-component values for fast and slow transverse relaxation. Therefore the estimates are not directly comparable with previous studies. However as the bi-exponential model can be envisaged as sampling T_2^* distribution at two discrete points, the fast and slow T_2^* estimates should lie reasonably close to mean T_2^* in voxels with relatively narrow T_2^* distributions. For example in CSF voxels without partial voluming, a relatively smaller number of compartments are observed and the mean T_2^* values are reasonably closer to the previous studies (11, 39, 37, 45). The wide spread of mean T_2^* distribution in CSF (Figure 5a) is due to strong partial volume effects present at low resolution, which are also present in GM and WM voxels, as suggested by the large overlap between empirical probability distributions. Given that the mean T_2^* combines contributions from both fast and slow transverse relaxation components in various compartmentalized motion regimes, the average mean T_2^* values of 5 ms (WM) and 7 ms (GM) lie expectedly in the range ($T_{2_{short}}^*$, $T_{2_{long}}^*$) derived from previously reported values (11, 39, 37, 45).

The continuum of components concept has recently been explored in the interpretation of sodium MRI data, where a regularised inverse Laplace transform was performed through least squares estimation, initialized by a trimodal distribution over a logarithmically-spaced pseudo-continuous grid of T_2^* values (40). This approach is similar to the nonparametric NNLS method (46), which divides the T_2 parameter space into a pseudo-continuous grid and employs a regularised non-negative linear least squares algorithm to estimate a T_2 distribution. On the same principle, Layton et al (47) proposed an inverse gamma mixture model to estimate the width of T_2 modes in multi-echo T_2-weighted proton MRI data. It has been shown in (47) that accurate estimation of the widths of the T_2 modes is challenging due to ill-posedness and regularization associated bias in the inferred distribution shape.

Continuum distribution models with gamma distribution have been used to describe the distribution of the Apparent Diffusion Coefficient (48, 49) in diffusion MRI data. The DIAMOND method allows for the accu-

rate and robust characterization of tridimensional anisotropic diffusitivity in tissue (49). In micro-structure imaging AxCaliber, a method for determining axon diameter distribution, assumes a gamma distributed axonal population in WM tissue, resulting in an intractable summation and necessitating the use of a grid-search algorithm for parameter estimation (50).

The continuum distribution model presented in this work assumes a unimodal T_2^* distribution. However, as sodium transverse relaxation is inherently two-component (41), the estimates of mean T_2^* will be biased towards the dominant relaxation component. Furthermore, the narrow T_2^* distribution in CSF, with strong partial volume effects at the tissue-CSF border, present additional challenges to robust parameter inference. The high SNR signal from CSF masks the weaker signal from tissue, resulting in skewed estimation of mean T_2^* and f_{fast} towards CSF. Similarly in pathological tissue, such as edema, the peak of the gamma distribution may be biased towards the CSF content. In future the signal model can be extended to incorporate multimodal T_2^* distributions, such as the gamma mixture distribution employed in DIAMOND (49), with an additional mono-exponential CSF component. However, the inherently ill-posed nature of mixture models leads to challenging estimation, which is prone to producing unrealistic and biased parameter estimates, as discussed in (47). Care must be taken to mitigate the impact of such effects on the estimation performance.

6 Conclusion

A continuum distribution model for characterizing transverse relaxation decay in ^{23}Na MRI signal is presented. We have demonstrated that the gamma distribution model outperforms the bi-exponential mixture model in terms of ease of implementation and interpretability. Furthermore, the gamma model provides robust parameter maps with more pronounced structural details. Given the flexibility offered by the gamma distribution model in characterizing a wide range of T_2^* component distributions and superior estimation performance under low SNR and large partial volume effects, we recommend use of the continuum distribution approach for the analysis of ^{23}Na-MRI data.

7 List of Figures

Figure 1: Schematic diagram of the image acquisition, estimation and evaluation pipeline.

Figure 2: (a) Parameter maps of BEM and GA models in phantom vials. (b) Parameter estimates (mean ± s.d.) across agar concentration for different ^{23}Na concentrations. $T_{2_{\mathrm{GA}}}^*$ maps clearly delineate different media.

Unlike BEM relaxation parameters, mean $T^*_{2_{\mathrm{GA}}}$ monotonically decreases with increasing agar concentration.

Figure 3: (a) Single voxel data (gray), overlaid with curve-fits from the mono-exponential, ME (green), bi-exponential, BE (blue) and continuum distribution, GA (black) models and (b) corresponding gamma pdfs in WM (V1), GM (V2) and CSF (V3). (c) Histogram of the difference map, ML_{GA}-ML_{BE}, for all voxels of subject 1.

Figure 4: Parameter maps estimated from the continuum distribution model ($T^*_{2_{\mathrm{GA}}}$, f_{fast}), and the bi-exponential mixture model ($T^*_{2_{\mathrm{short}}}$, $T^*_{2_{\mathrm{long}}}$).

Figure 5: (a) Empirical pdf of $T^*_{2_{\mathrm{GA}}}$ from voxelwise estimation of the gamma distribution in CSF (black), GM (cyan) and WM (blue). (b) Empirical pdfs of fast decay fraction, f_{fast}, in CSF (black), GM (cyan) and WM (blue).

Figure 6: Fast fraction maps at different threshold values.

8 Acknowledgements

This work was supported by Australian Research Council Discovery Project DP110103292. The authors acknowledge the technical and scientific support of the Australian National Imaging Facility at the Melbourne Brain Centre Imaging Unit.

References

1. Isom LL. The role of sodium channels in cell adhesion. Frontiers in Bioscience 7 2002;53(3):12–23.
2. Dean RB. Theories of electrolyte equilibrium in muscle. In: Biol. Symp vol. 3; 1941. p. 331–348.
3. Horisberger JD. Recent Insights into the Structure and Mechanism of the Sodium Pump. Physiology 2004;19(6):377–387.
4. Smith JR, Gheorghiade M, Goldstein S. The current role of digoxin in the treatment of heart failure. Coronary Artery Disease 1993;4(1):16–26.
5. Schmidt TA, Allen PD, Colucci WS, Marsh JD, Kjeldsen K. No adaptation to digitalization as evaluated by digitalis receptor (Na, K-ATPase) quantification in explanted hearts from donors without heart

disease and from digitalized recipients with end-stage heart failure. The American Journal of Cardiology 1993;71(1):110–114.

6. Graves SW, Brown B, Valdes R. An endogenous digoxin-like substance in patients with renal impairment. Annals of Internal Medicine 1983;99(5):604–608.

7. Christo PJ, El-Mallakh RS. Possible role of endogenous Ouabain-like compounds in the pathophysiology of bipolar illness. Medical Hypotheses 1993;41(4):378–383.

8. El-Mallakh RS, Barrett JL, Jed-Wyatt R. The Na, K-ATPase hypothesis for bipolar disorder: Implications of normal development. Journal of Child and Adolescent Psychopharmacology 1993;3(1):37–52.

9. Clerico A, Giampietro O. Is the endogenous digitalis-like factor the link between hypertension and metabolic disorders as diabetes mellitus, obesity and acromegaly? Clinical Physiology and Biochemistry 1990;8(3):153–168.

10. Rose AM, Valdes R. Understanding the sodium pump and its relevance to disease. Clinical Chemistry 1994;40(9):1674–1685.

11. Madelin G, Regatte RR. Biomedical applications of sodium MRI in vivo. Journal of Magnetic Resonance Imaging 2013;38(3):511–529.

12. Hilal SK, Maudsley AA, Ra J, Simon HE, Roschmann P, Wittekoek S, Cho Z, Mun S. In vivo NMR imaging of sodium-23 in the human head. Journal of Computer Assisted Tomography 1985;9(1):1–7.

13. Grodd W, Klose U. Sodium-MR-imaging of the brain: initial clinical results. Neuroradiology 1988;30(5):399–407.

14. Hancu I, Boada FE, Shen GX. Three-dimensional triple-quantum–filtered ^{23}Na imaging of in vivo human brain. Magn Reson Med 1999;42(6):1146–1154.

15. Rosen Y, Lenkinski RE. Sodium MRI of a human transplanted kidney. Academic Radiology 2009;16(7):886–889.

16. Hashimoto T, Ikehira H, Fukuda H, Yamaura A, Watanabe O, Tateno Y, Tanaka R, Simon H. In vivo sodium-23 MRI in brain tumors: evaluation of preliminary clinical experience. American Journal of Physiologic Imaging 1991;6(2):74–80.

17. Ouwerkerk R, Bleich KB, Gillen JS, Pomper MG, Bottomley PA. Tissue sodium concentration in human brain tumors as measured with ^{23}Na MR imaging. Radiology 2003;227(2):529–537.

18. Nagel AM, Bock M, Hartmann C, Gerigk L, Neumann JO, Weber MA, Bendszus M, Radbruch A, Wick W, Schlemmer HP, et al. The potential of relaxation-weighted sodium magnetic resonance imaging as demonstrated on brain tumors. Investigative Radiology 2011;46(9):539–547.

19. Fiege DP, Romanzetti S, Mirkes CC, Brenner D, Shah NJ. Simultaneous single-quantum and triple-quantum-filtered MRI of ^{23}Na (SISTINA). Magn Reson Med 2013;69(6):1691–1696.

20. Tsang A, Stobbe RW, Asdaghi N, Hussain MS, Bhagat YA, Beaulieu C, Emery D, Butcher KS. Relationship between sodium intensity and perfusion deficits in acute ischemic stroke. Journal of Magnetic Resonance Imaging 2011;33(1):41–47.

21. Inglese M, Madelin G, Oesingmann N, Babb J, Wu W, Stoeckel B, Herbert J, Johnson G. Brain tissue sodium concentration in multiple sclerosis: a sodium imaging study at 3 Tesla. Brain 2010;133(3):847–857.

22. Zaaraoui W, Konstandin S, Audoin B, Nagel AM, Rico A, Malikova I, Soulier E, Viout P, Confort-Gouny S, Cozzone PJ, et al. Distribution of brain sodium accumulation correlates with disability in multiple sclerosis: a cross-sectional ^{23}Na MR imaging study. Radiology 2012;264(3):859–867.

23. Mellon E, Pilkinton D, Clark C, Elliott M, Witschey W, Borthakur A, Reddy R. Sodium MR imaging detection of mild Alzheimer disease: preliminary study. American Journal of Neuroradiology 2009;30(5):978–984.

24. Reetz K, Romanzetti S, Dogan I, Saß C, Werner CJ, Schiefer J, Schulz JB, Shah NJ. Increased brain tissue sodium concentration in Huntington's Diseasea sodium imaging study at 4 T. NeuroImage 2012;63(1):517–524.

25. Ouwerkerk R, Jacobs MA, Macura KJ, Wolff AC, Stearns V, Mezban SD, Khouri NF, Bluemke DA, Bottomley PA. Elevated tissue sodium concentration in malignant breast lesions detected with non-invasive ^{23}Na MRI. Breast Cancer Research and Treatment 2007;106(2):151–160.

26. Jerecic R, Bock M, Wacker C, Bauer W, Schad L. ^{23}Na-MRI of the human heart using a 3D radial projection technique. Biomedizinische Technik/Biomedical Engineering 2002;47(s1a):458–459.

27. Parish TB, Fieno DS, Fitzgerald SW, Judd RM. Theoretical basis for sodium and potassium MRI of the human heart at 1.5 T. Magn Reson Med 1997;38(4):653–661.

28. Ouwerkerk R, Weiss RG, Bottomley PA. Measuring human cardiac tissue sodium concentrations using surface coils, adiabatic excitation, and twisted projection imaging with minimal T_2 losses. Journal of Magnetic Resonance Imaging 2005;21(5):546–555.

29. Ouwerkerk R, Bottomley PA, Solaiyappan M, Spooner AE, Tomaselli GF, Wu KC, Weiss RG. Tissue Sodium Concentration in Myocardial Infarction in Humans: A Quantitative ^{23}Na MR Imaging Study. Radiology 2008;248(1):88–96.

30. Chang G, Wang L, Schweitzer ME, Regatte RR. 3D ^{23}Na MRI of human skeletal muscle at 7 Tesla: initial experience. European Radiology 2010;20(8):2039–2046.

31. Wheaton AJ, Borthakur A, Shapiro EM, Regatte RR, Akella SV, Kneeland JB, Reddy R. Proteoglycan loss in human knee cartilage: quantitation with sodium MR imagingfeasibility study. Radiology 2004;231(3):900–905.

32. Maril N, Rosen Y, Reynolds GH, Ivanishev A, Ngo L, Lenkinski RE. Sodium MRI of the human kidney at 3 Tesla. Magn Reson Med 2006;56(6):1229–1234.

33. Madelin G, Lee J, Regatte RR, Jerschow A. Sodium MRI: Methods and applications. Progress in Nuclear Magnetic Resonance Spectroscopy 2014;79(Supplement C):14 – 47.

34. Berendsen H, Edzes H. The observation and general interpretation of sodium magnetic resonance in biological material. Annals of the New York Academy of Sciences 1973;204(1):459–485.

35. Freed JH. Generalized Cumulant Expansions and Spin-Relaxation Theory. The Journal of Chemical Physics 1968;49(1):376–391.

36. Eliav U, Navon G. Analysis of double-quantum-filtered NMR spectra of ^{23}Na in biological tissues. Journal of Magnetic Resonance, Series B 1994;103(1):19–29.

37. Ridley B, Nagel AM, Bydder M, Maarouf A, Stellmann JP, Gherib S, Verneuil J, Viout P, Guye M, Ranjeva JP, et al. Distribution of brain sodium long and short relaxation times and concentrations: a multi-echo ultra-high field ^{23}Na MRI study. Scientific reports. 2018;8(1):4357.

38. Niesporek SC, Umathum R, Fiedler TM, Bachert P, Ladd ME, Nagel AM. Improved T_2^* determination in ^{23}Na, ^{35}Cl, and ^{17}O MRI using iterative partial volume correction based on ^{1}H MRI segmentation. Magnetic Resonance Materials in Physics, Biology and Medicine. 2017;30(6):519–536.

39. Blunck Y, Josan S, Taqdees SW, Moffat BA, Ordidge RJ, Cleary JO, Johnston LA. 3D-multi-echo radial imaging of ^{23}Na (3D-MERINA) for time-efficient multi-parameter tissue compartment mapping. Magn Reson Med 2018;79(4):1950–1961.

40. Riemer F, Solanky BS, Wheeler-Kingshott CA, Golay X. Bi-exponential ^{23}Na T_2^* component analysis in the human brain. NMR in Biomedicine. 2018;31(5):e3899.

41. Hubbard PS. Nonexponential Nuclear Magnetic Relaxation by Quadrupole Interactions. The Journal of Chemical Physics 1970;53(3):985–987.

42. Jenkinson M, Beckmann CF, Behrens TE, Woolrich MW, Smith SM. FSL. NeuroImage 2012;62(2):782–790.

43. Gudbjartsson H, Patz S. The Rician distribution of noisy MRI data. Magn Reson Med. 1995;34(6):910–914.

44. Celik H, Bouhrara M, Reiter DA, Fishbein KW, Spencer RG. Stabilization of the inverse Laplace transform of multiexponential decay through introduction of a second dimension. Journal of Magnetic Resonance 2013;236:134–139.

45. Lommen JM, Flassbeck S, Behl NG, Niesporek S, Bachert P, Ladd ME, Nagel AM. Probing the microscopic environment of ^{23}Na ions in brain tissue by MRI: On the accuracy of different sampling schemes for the determination of rapid, biexponential decay at low signal-to-noise ratio. Magnetic resonance in medicine. 2018;80(2):571–584.

46. Whittall KP, MacKay AL. Quantitative interpretation of NMR relaxation data. Journal of Magnetic Resonance (1969) 1989;84(1):134 – 152.

47. Layton KJ, Morelande M, Wright D, Farrell PM, Moran B, Johnston LA. Modelling and estimation of multicomponent T_2 distributions. IEEE Transactions on Medical Imaging 2013;32(8):1423–1434.

48. Yablonskiy DA, Bretthorst GL, Ackerman JH. Statistical Model for Diffusion Attenuated MR Signal. Magn Reson Med. 2003;50(4):664–669.

49. Scherrer B, Schwartzman A, Taquet M, Sahin M, Prabhu SP, Warfield SK. Characterizing Brain Tissue by Assessment of the Distribution of Anisotropic Microstructural Environments in Diffusion-Compartment Imaging (DIAMOND). Magn Reson Med. 2016;977:963–977.

50. Assaf Y, Blumenfeld-Katzir T, Yovel Y, Basser PJ. AxCaliber: a method for measuring axon diameter distribution from diffusion MRI. Magn Reson Med. 2008;59(6):1347–1354.

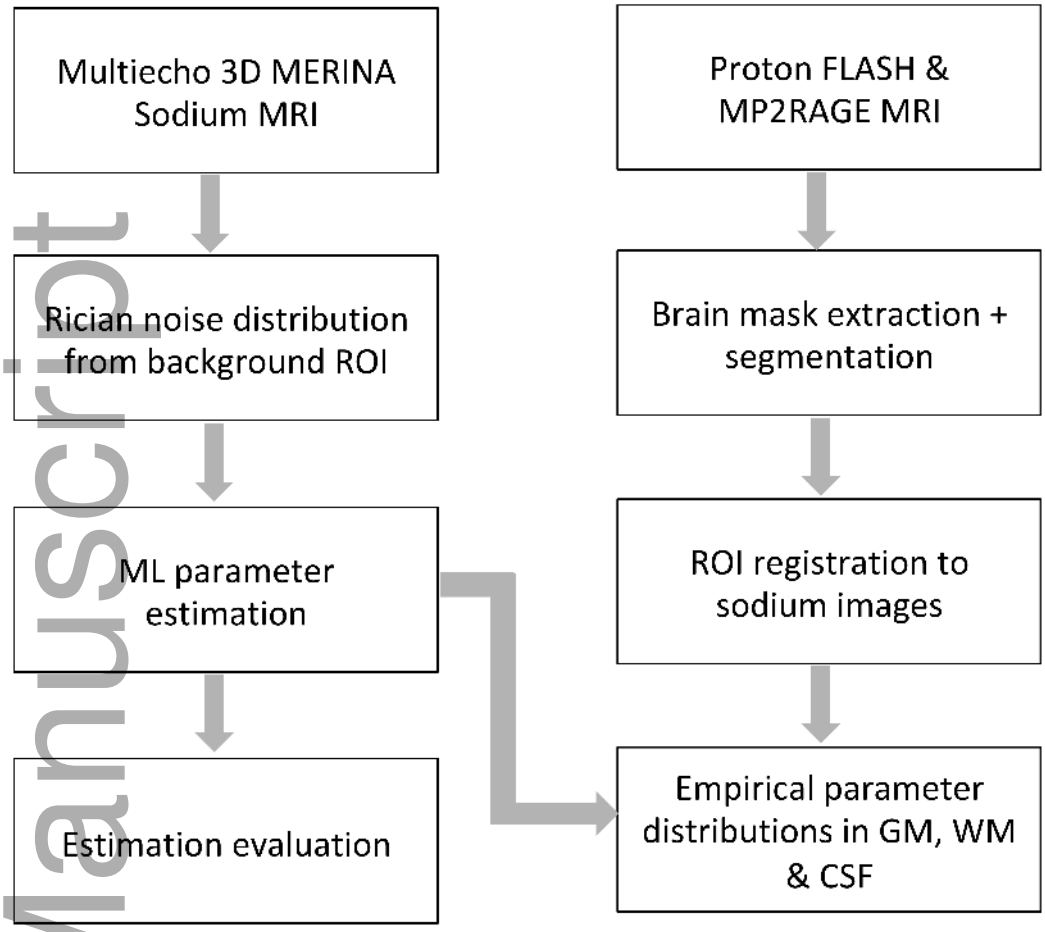

mrm_27659_f1.tiff

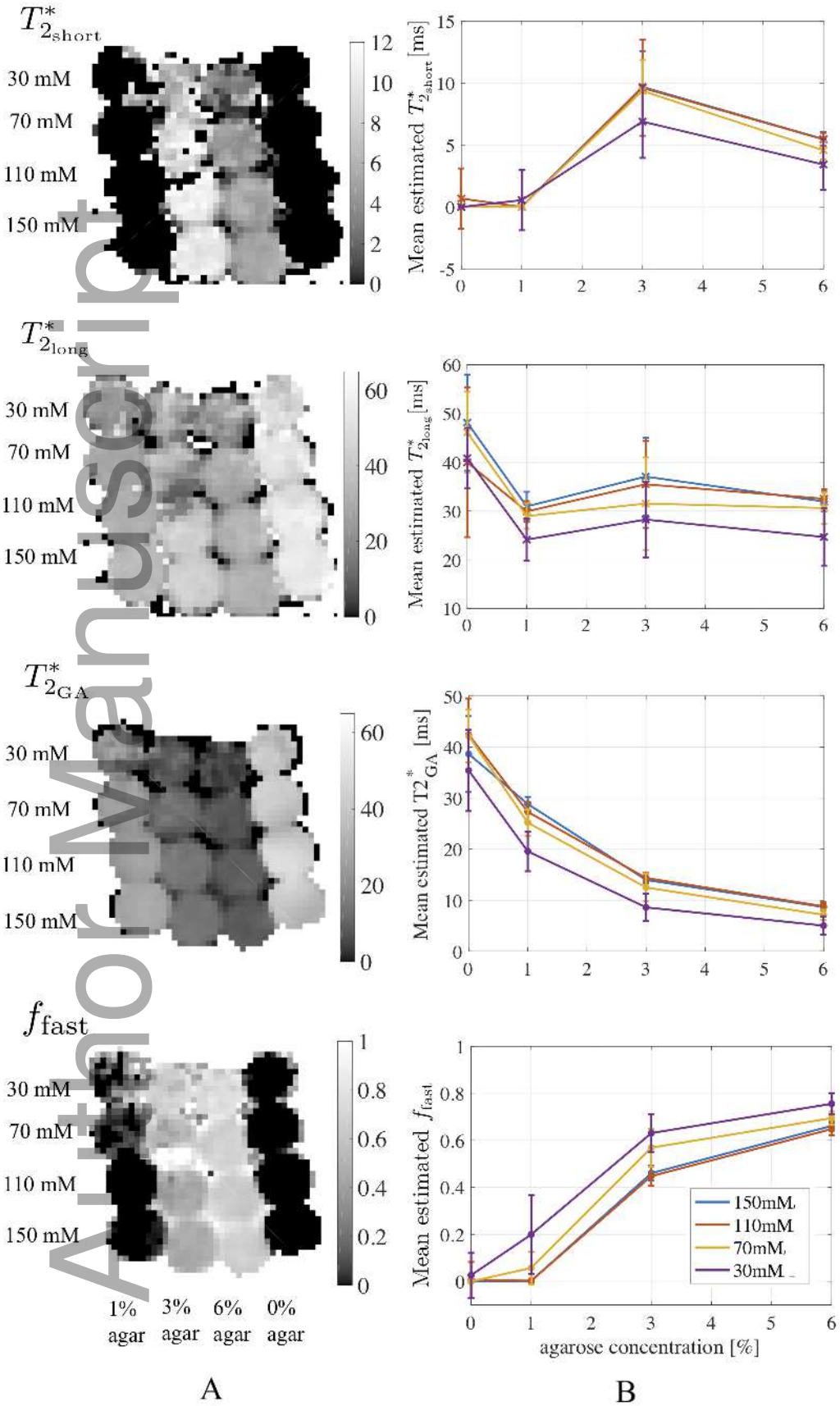

mrm_27659_f2.tiff

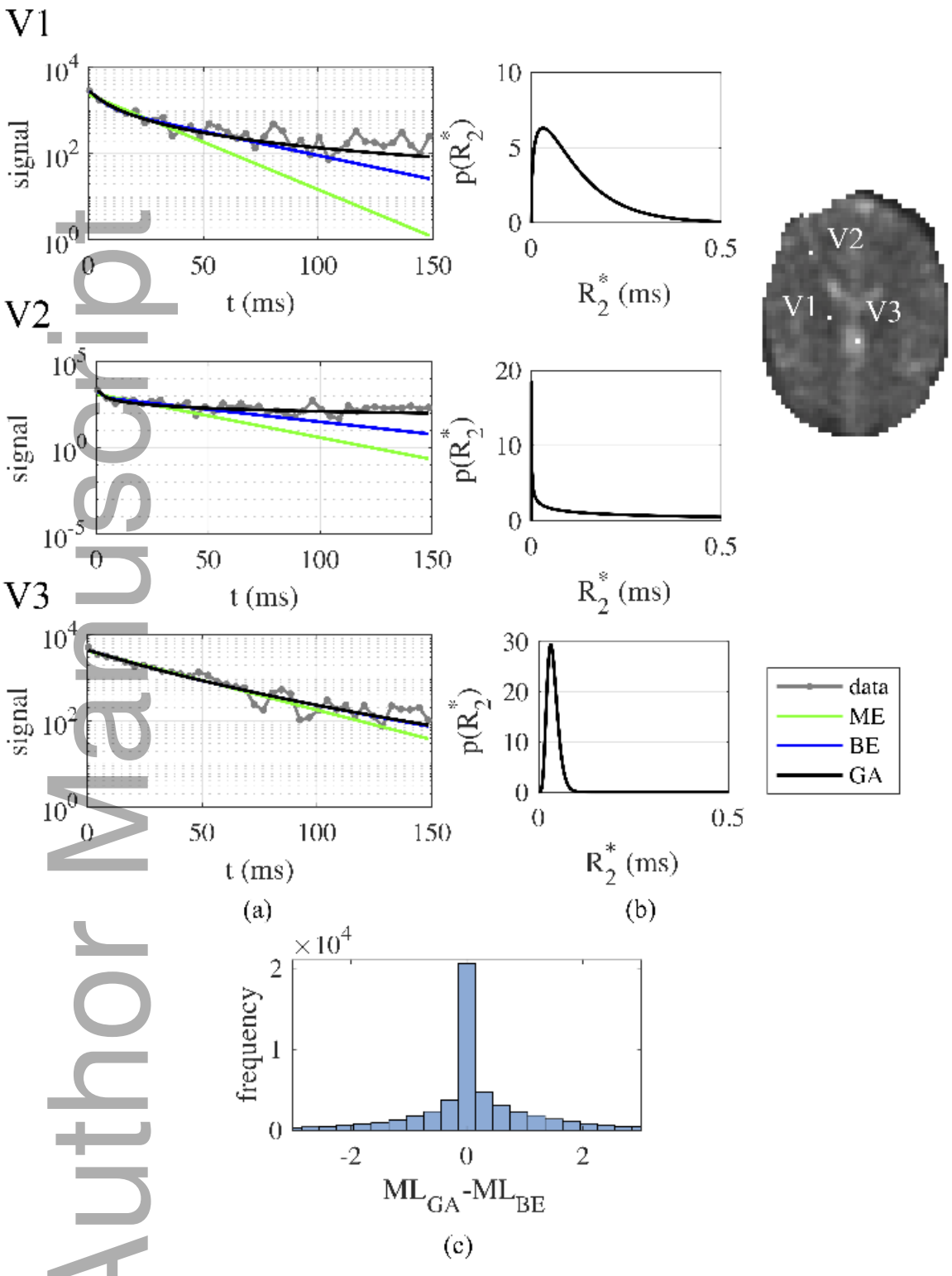

mrm_27659_f3.tiff

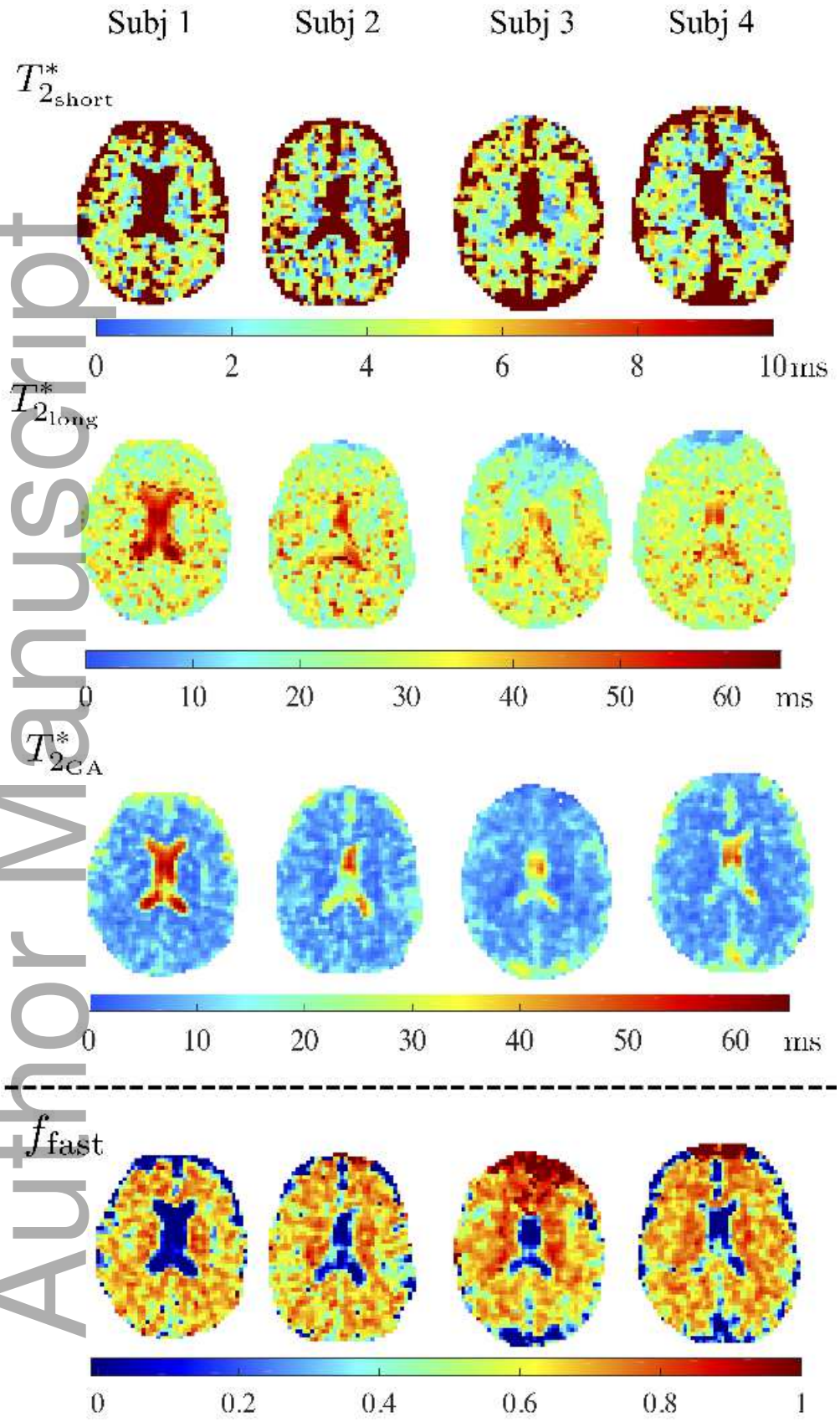

mrm_27659_f4.tiff

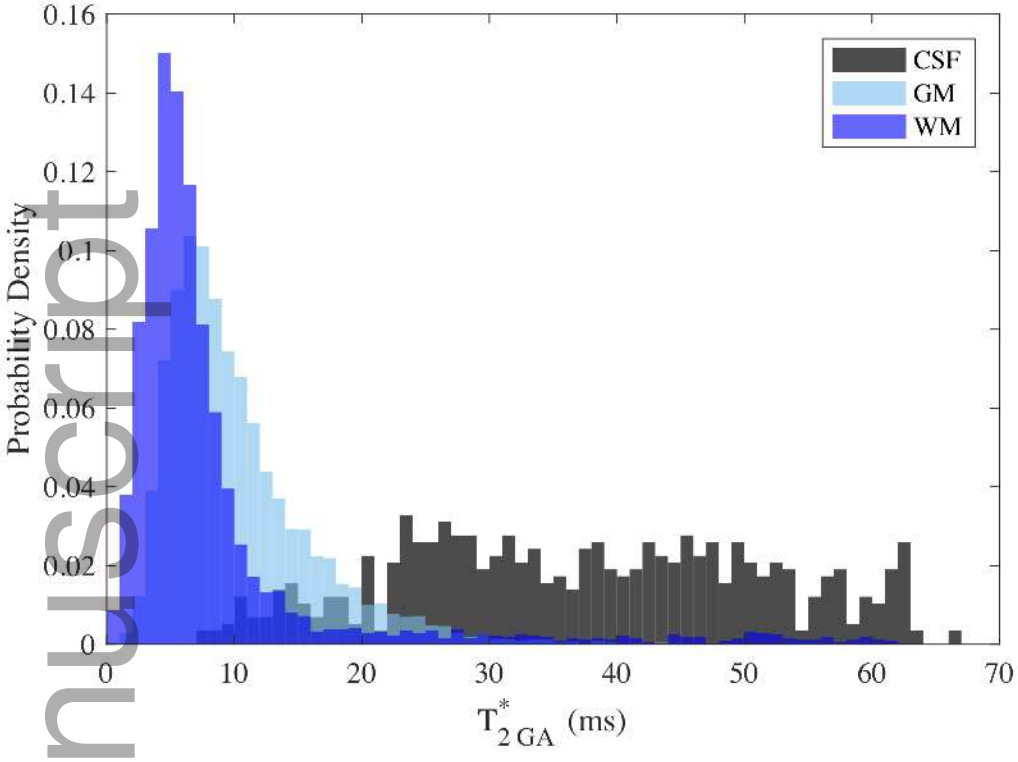

(a)

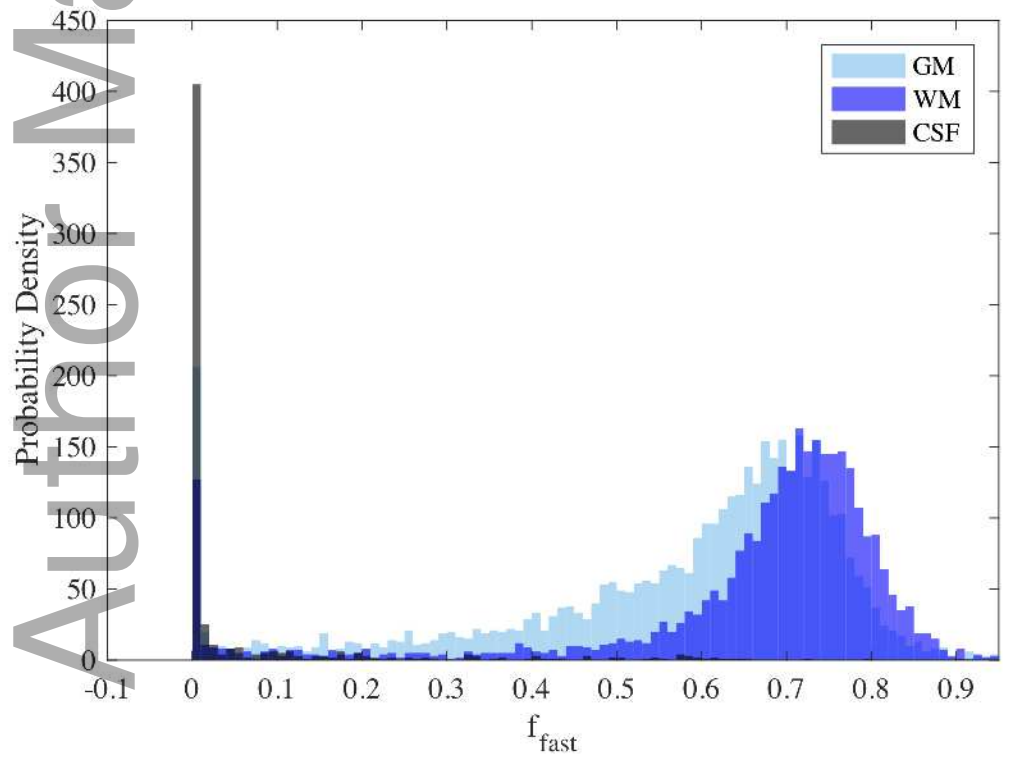

(b)

mrm_27659_f5.tiff

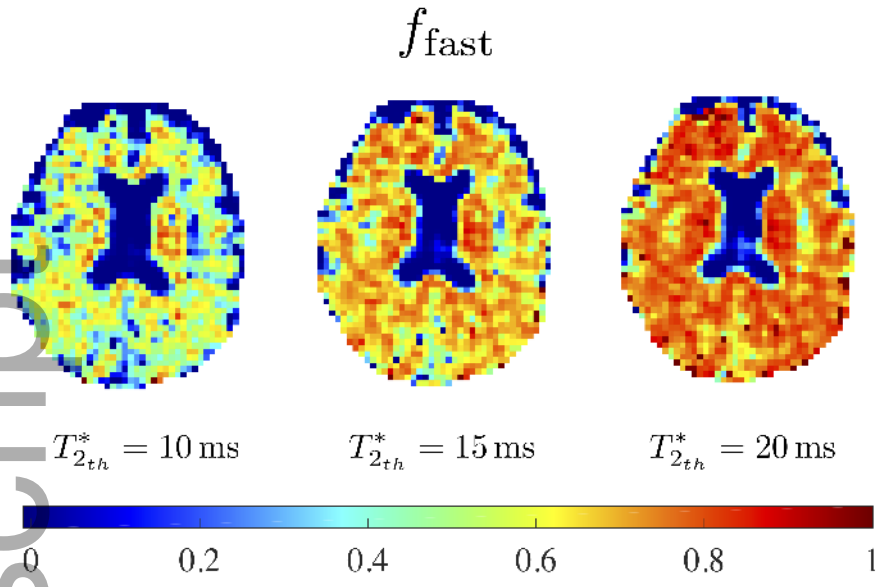

mrm_27659_f6.tiff